Exploring the protective mechanisms and therapeutic potential of carnosic acid against acute respiratory distress syndrome through molecular docking, molecular dynamics and experimental verification

QUAN LI[1*], LILI DING[1*], HAIJUN SUN[1*], WEICHAO DING[2], MENGMENG WANG[3], ZHAORUI SUN[3] and CONGXUE MA[4]

[1]Intensive Care Unit, Suqian First Hospital, Suqian, Jiangsu 223800, P.R. China; [2]Department of Emergency Medicine, The Affiliated Hospital of Xuzhou University, Xuzhou, Jiangsu 221002, P.R. China; [3]Department of Emergency Medicine, Medical School of Nanjing University Affiliated Jinling Hospital, Nanjing, Jiangsu 210002, P.R. China; [4]Department of Anesthesiology, Siyang Hospital, Suqian, Jiangsu 223700, P.R. China

Received May 7, 2025; Accepted December 30, 2025

DOI: 10.3892/etm.2026.13077

Abstract. In the present study, a method combining network pharmacology prediction and experimental verification was used to clarify the protective mechanisms and therapeutic benefits of carnosic acid (CA) against acute respiratory distress syndrome (ARDS). Network pharmacology analysis was initially carried out to identify key targets and pathways for CA in ARDS. *In vitro* studies were performed using mouse alveolar macrophages (MH-S cells) to examine the impact of CA on pyroptosis and oxidative stress triggered by lipopolysaccharide (LPS)/ATP. Pyroptosis was evaluated through Annexin V/PI staining, measurement of IL-1β and IL-18 levels, and expression analysis of pyroptosis-related genes. Assessment of oxidative stress involved measuring malondialdehyde, myeloperoxidase and superoxide dismutase levels, as well as intracellular reactive oxygen species (ROS) levels. Western blotting and immunofluorescence analysis were employed to investigate nuclear factor erythroid 2-related factor 2 (Nrf2) expression and nuclear translocation. Additionally, an *in vivo* ARDS mouse model was developed to further validate the therapeutic efficacy of CA through assessment of lung injury, inflammation and oxidative stress markers. Network pharmacology profiling revealed Nrf2 as the pivotal molecular target of CA, with pathway enrichment analysis highlighting its involvement in ROS homeostasis and programmed cell death pathways. Molecular docking analysis demonstrated a stable binding affinity between CA and Nrf2. *In vitro* experimental analysis revealed that CA notably reduced LPS/ATP-induced pyroptosis and oxidative stress, therefore reducing apoptosis, downregulating pyroptosis-related gene expression, and enhancing Nrf2 expression and nuclear translocation in MH-S cells. *In vivo* validation in the murine ARDS model demonstrated that CA treatment effectively mitigated pulmonary pathological damage, suppressed pyroptotic signaling pathways and reduced oxidative stress biomarkers. The present integrative study demonstrated that CA may protect against ARDS by targeting Nrf2, suppressing oxidative stress and pyroptosis. These findings provide a mechanistic understanding of CA and warrant further translational research for clinical application in ARDS management.

Introduction

Acute respiratory distress syndrome (ARDS) is a life-threatening pulmonary disorder characterized by uncontrolled inflammatory responses, diffuse alveolar damage and increased pulmonary vascular permeability, leading to severe impairment of gas exchange and potentially fatal respiratory failure (1). Despite significant advances in supportive care, primarily involving lung-protective ventilation strategies and refined fluid management, the mortality rate of ARDS remains unacceptably high, ranging from 35 to 46% (2). The current therapeutic landscape lacks effective pharmacological agents that directly target these underlying pathological mechanisms, highlighting a critical unmet need for novel therapeutic interventions (3).

In recent years, natural products derived from medicinal plants have garnered significant attention as promising sources for drug discovery due to their multi-target activities and favorable safety profiles (4). Carnosic acid (CA), a phenolic

Correspondence to: Professor Congxue Ma, Department of Anesthesiology, Siyang Hospital, 26 Zhongxing Middle Road, Siyang, Suqian, Jiangsu 223700, P.R. China
E-mail: tougaoyouixang@126.com

*Contributed equally

Key words: acute respiratory distress syndrome, carnosic acid, nuclear factor erythroid 2-related factor 2, pyroptosis, network pharmacology, oxidative stress

diterpene abundantly found in rosemary (*Rosmarinus officinalis Linnaeus*) and sage, has been extensively documented for its potent anti-inflammatory, antioxidant and antimicrobial properties (5). Previous studies have demonstrated that CA can activate the nuclear factor erythroid 2-related factor 2 (Nrf2) pathway, a master regulator of cellular antioxidant responses. Upon activation, Nrf2 translocates to the nucleus and induces the expression of a battery of cytoprotective genes, including heme oxygenase-1 (HO-1), which collectively counteract oxidative stress (6,7). Furthermore, evidence suggests that Nrf2 activation can indirectly suppress the NLR family pyrin domain containing 3 (NLRP3) inflammasome, a key component of innate immunity whose hyperactivation drives pyroptosis, a highly inflammatory form of programmed cell death, through caspase-1-mediated cleavage of gasdermin D (GSDMD) and subsequent release of IL-1β and IL-18 (8,9). This Nrf2-NLRP3 axis has been implicated in various inflammatory diseases but remains relatively unexplored in the context of ARDS.

Given the central roles of oxidative stress and NLRP3 inflammasome-mediated pyroptosis in the pathogenesis of ARDS (10,11), we hypothesize that CA may confer protective effects against this syndrome. However, a systematic investigation into the therapeutic potential and precise molecular mechanisms of CA in ARDS, particularly its potential to simultaneously modulate the Nrf2 pathway and NLRP3-mediated pyroptosis, is still lacking.

Therefore, the present study employed an integrative approach combining network pharmacology prediction, molecular docking, molecular dynamics (MD) simulations and experimental verification to elucidate the protective mechanisms and therapeutic benefits of CA against ARDS. The study aims to provide a solid foundation for the further development of CA as a potential therapeutic agent for ARDS.

Materials and methods

Network pharmacology analysis

Data preparation. Potential targets for CA were predicted using the SwissTargetPrediction database (http://www.swisstargetprediction.ch). ARDS-related targets were identified using public databases, including the GeneCards database (https://www.genecards.org/) and the DisGeNET database (version 7.0; http://www.disgenet.org/). To identify relevant targets, the search terms 'ARDS', 'acute lung injury', 'acute respiratory distress syndrome', 'adult respiratory distress syndrome' and 'acute lung injury' were used. In the GeneCards database, target selection was carried out using the following criteria: i) Ranking targets by their relevance score; ii) retaining only those with a score >2 times the median value and iii) identifying and presenting the common targets between CA and ARDS using a Venn diagram.

Functional enrichment analysis. Metascape (http://www.metascape.org) is an online tool for functional annotation. This platform facilitates gene function annotation analysis, empowering users to leverage contemporary, prevalent bioinformatics methodologies in the examination of gene and protein batches. By doing so, it enables the elucidation of gene and protein functionalities (12). The tool was used to carry out a functional enrichment analysis of the intersected target genes using Gene Ontology (GO) (13) and Kyoto Encyclopedia of Genes and Genomes (KEGG) pathway analyses (14). The GO analysis encompassed three categories: i) Biological processes (BP); ii) molecular functions (MF); and iii) cellular components (CC). The top 10 most significantly enriched terms in both GO-BP and KEGG pathway analyses were then visualized using the SRplot bioinformatics platform (http://www.bioinformatics.com.cn/; last accessed on April 1, 2025). $P<0.05$ was considered to indicate a statistically significant difference.

Protein-protein interaction (PPI) network construction. Overlapping targets were analyzed using Search Tool for the Retrieval of Interacting Genes/Proteins (STRING; https://cn.string-db.org/; version 11.0) to construct a PPI network. This network was constructed with a specific focus on *Homo sapiens* and a high confidence score of 0.950 to ensure the reliability of interactions. Following this, the PPI network was visually rendered using Cytoscape software (version 3.7.2) (15), facilitating a comprehensive visualization and analysis of the intricate protein interactions.

Molecular docking. Molecular docking has emerged as a fundamental technique in modern drug discovery, allowing researchers to predict binding affinities and molecular interactions by analyzing the three-dimensional conformations of protein-ligand complexes. In the present study, molecular docking simulations were carried out between CA and its key target proteins identified through the aforementioned analysis. The three-dimensional structures of CA and the pivotal proteins were sourced from PubChem (https://pubchem.ncbi.nlm.nih.gov/) and the Research Collaboratory for Structural Bioinformatics Protein Data Bank database (http://www.rcsb.org/). All docking procedures were executed using AutoDock Tools (version 1.5.6; https://autodock.scripps.edu/), with validation steps incorporated to verify the reliability of the computational predictions. Analysis of molecular docking utilized binding energy to assess protein-ligand interactions, with values ≤-5 kcal/mol indicating strong binding affinity (16). To assess structural alignment, root mean square deviation (RMSD) calculations were employed. The RMSD lower bound (RMSD l.b.) and the RMSD upper bound (RMSD u.b.) allow the diversity of conformations in the molecular docking results, and the deviation range from the target conformation to be understood. This is useful for evaluating the reliability and accuracy of the docking results. Generally, the smaller the RMSD l.b., the more similar the conformation obtained from the docking is to the target conformation, and the more reliable the docking result is. Conversely, the RMSD u.b. can assist in determining whether the docking algorithm is capable of searching a sufficiently wide enough conformational space. To facilitate a deeper understanding of the docking results, the molecular docking patterns were visually represented using PyMOL software (version 2.4; https://www.pymol.com/pymol.html), allowing for a detailed examination of the interactions at a molecular level.

MD. Groningen Machine for Chemical Simulations (GROMACS; version 2022.4; http://www.gromacs.org) was used to carry out MD simulations, which were all executed under isothermal-isobaric ensemble conditions simulating a system with a constant number of particles, temperature and pressure (NPT) with periodic boundary constraints. The linear constraint solver algorithm constrained hydrogen

Table I. Reagents and antibodies.

Name	Catalogue number	Manufacturer
CA	B21175	Shanghai Yuanye Biotechnology Co., Ltd.
LPS (0111:B4)	L4391	Sigma Aldrich; Merck KGaA
ML385	HY-100523	MEDCHEMEXPRESS LLC
DMEM	12100	Beijing Solarbio Science & Technology Co., Ltd.
RIPA Buffer	R0010	Beijing Solarbio Science & Technology Co., Ltd.
ATP	A9310	Beijing Solarbio Science & Technology Co., Ltd.
NLRP3 antibody	15101	Cell Signaling Technology, Inc.
ASC antibody	67824	Cell Signaling Technology, Inc.
CASP1 antibody	24232	Cell Signaling Technology, Inc.
GSDMD antibody	39754	Cell Signaling Technology, Inc.
Nrf2 antibody	12721	Cell Signaling Technology, Inc.
HO-1 antibody	43966	Cell Signaling Technology, Inc.
GAPDH antibody	2118	Cell Signaling Technology, Inc.
Secondary antibody	7074	Cell Signaling Technology, Inc.
Fluorescent secondary antibody	8889	Cell Signaling Technology, Inc.
IL-1β ELISA	E-EL-R0012c	Wuhan Elabscience Biotechnology Co., Ltd.
IL-18 ELISA	SEA064Ra	Wuhan Elabscience Biotechnology Co., Ltd.
MDA assay kit	A003-1-2	Nanjing Jiancheng Bioengineering Institute
MPO assay kit	A044-1-1	Nanjing Jiancheng Bioengineering Institute
SOD assay kit	A001-3-2	Nanjing Jiancheng Bioengineering Institute
LDH assay kit	C0016	Beyotime Biotechnology
Annexin V-FITC/PI	APOAF	Sigma Aldrich; Merck KGaA
DCFH-DA	S0033	Beyotime Biotechnology
Goat serum	C0265	Beyotime Biotechnology
BCA	PC0020	Beijing Solarbio Science & Technology Co., Ltd.
CCK-8	C0037	Beyotime Biotechnology
RT-qPCR kit	D7268S	Beyotime Biotechnology

CA, carnosic acid; LPS, lipopolysaccharide; NLRP3, NLR family pyrin domain containing 3; ASC, apoptosis-associated speck-like protein containing a CARD; CASP1, caspase-1; GSDMD, gasdermin D; Nrf2, nuclear factor erythroid 2-related factor 2; HO-1, heme oxygenase-1; MDA, malondialdehyde; MPO, myeloperoxidase; SOD, superoxide dismutase; LDH, lactate dehydrogenase; DCFH-DA, 2',7'-dichlorodihydrofluorescein diacetate; CCK-8, cell counting kit-8; RT-qPCR, reverse transcription-quantitative PCR.

bonds with a 2 fsec integration time step. Electrostatic energy (ELE) interactions were calculated using the particle-mesh Ewald method, with a 1.2-nm cutoff (17), while van der Waals (VDW) interactions employed a 10 Å cutoff distance, updated every 10 steps. Temperature (298 K) and pressure (1 bar) were maintained using the V-rescale thermostat and Berendsen barostat algorithms, respectively (18). The system underwent sequential equilibration under the protocol of 100 ps (constant number of particles, volume and temperature) followed by 100 ps NPT, before a 100 ns production run, with trajectories saved every 10 ps. Post-simulation analyses included trajectory visualization using Visual Molecular Dynamics (https://www.ks.uiuc.edu/Research/vmd/) and PyMOL, along with binding free energy calculations using the GROMACS package 'g_mmpbsa' (19). Key evaluation metrics comprised: i) System stability parameters (RMSD of complex protein and ligand; radius of gyration of complex; root mean square fluctuation of protein residues); ii) interaction characteristics (binding site distance, buried solvent-accessible surface area, VDW/ELE energies, hydrogen bond dynamics and per-residue energy contributions); and iii) structural features (conformational superposition and interaction fingerprints). This comprehensive analysis protocol ensured rigorous assessment of the protein-ligand complex dynamics.

Experimental design

Reagents and antibodies. Most of the reagents and antibodies used in the present study are shown in Table I.

Animals and treatments. Male BALB/c mice (n=48; age, 8 weeks; weight, 21-25 g), were obtained from the Model Animal Research Center of Nanjing University. Mice were housed in a standard laboratory environment maintained at a temperature range of 20-26˚C, with a relative humidity of 40-70% and a 12-h light/dark cycle. The mice were allowed to feed and drink *ad libitum* throughout the present study. All animal experiments were approved by the Institutional Ethics Committee of Medical School of Nanjing University Affiliated Jinling Hospital (Nanjing, China; approval

no. 2022DZGKJDWLS-00161) and complied with the Guide for the Care and Use of Laboratory Animals (https://olaw.nih.gov/policies-laws/guide-care-use-lab-animals).

The ARDS model was established through intraperitoneal (i.p.) injection of lipopolysaccharide (LPS; 10 mg/kg), a well-established method documented in previous studies (20,21). Mice were randomly allocated into the following four experimental groups (n=6/group): i) Control group (PBS; i.p.); ii) LPS group (10 mg/kg; i.p.); iii) CA group (40 mg/kg; i.p.); and iv) ML385 group (40 mg/kg CA + 30 mg/kg ML385; i.p.). All animals were anesthetized with 1% sodium pentobarbital (40 mg/kg; i.p.) before administration. A total of 30 min post-LPS injection, treatment groups received either CA (dissolved in 0.5% DMSO) or the combination of ML385 [nuclear factor erythroid 2-related factor 2 (Nrf2) inhibitor; dissolved in 0.5% DMSO; 30 mg/kg, i.p.] (22) followed by CA, while controls received equivalent volumes of PBS. Survival rates were recorded every 24 h for a 7-day observation period following the LPS challenge. Animal deaths were checked for twice daily (morning and evening) using a combination of criteria: i) The absence of spontaneous movement for >5 min of observation; ii) the lack of a response to gentle tactile stimuli (e.g., a soft touch with a clean gloved finger); and iii) the absence of visible respiration and signs of a heartbeat. For mice reaching the predefined moribund state (severe lethargy, inability to rise, dyspnea, etc.), euthanasia was performed promptly with an overdose of sodium pentobarbital (100 mg/kg, i.p.), and the time of euthanasia was recorded as the time of death for survival analysis. Upon confirmation of death, a necropsy was immediately performed. The thoracic cavity was exposed, and the lung tissues were carefully excised en bloc. Subsequently, the lungs were perfused via the trachea with ice-cold phosphate-buffered saline (PBS) to clear residual blood. After blotting the surface liquid with filter paper, the tissues were processed according to downstream experimental needs: The left lung lobe was fixed in 4% paraformaldehyde at 4˚C for 24 h for histological analysis, while the right lung lobe was snap-frozen in liquid nitrogen and then transferred to a -80˚C freezer for storage, and reserved for subsequent protein or RNA extraction. All tissue samples were maintained at -80˚C until use.

Following euthanasia, 0.6-0.8 ml left ventricular blood was immediately collected for blood gas analysis testing of arterial oxygen partial pressure (PaO_2) levels and arterial carbon dioxide partial pressure ($PaCO_2$), FiO_2 was measured during sampling using an oxygen monitor. The PaO_2/FiO_2 ratio was then calculated as PaO_2 (mmHg) divided by FiO_2. Bronchoalveolar lavage fluid (BALF) was obtained by carrying out three cycles of instillation and withdrawal with 1-ml sterile PBS through a tracheal cannula. The BALF samples were centrifuged at 1,500 x g for 15 min at 4˚C and the resulting supernatant was aliquoted and stored at -80˚C for subsequent cytokine analysis. For histological examination, the left lung lobes were perfused with PBS and fixed in 4% paraformaldehyde at 4˚C for 24 h before paraffin embedding. Tissue sections (4-μm thick) were prepared and stained with H&E using standard protocols (hematoxylin: 0.1%, 5-8 min, room temperature; eosin: 0.5%, 1-3 min, room temperature). Lung pathology was examined under a light microscope (Olympus BX53) by an observer blinded to the groupings. Lung injury scores were graded using the following scale: 0, no injury; 2, mild injury (up to 25% injury of the field of view); 4, moderate injury (up to 50% injury of the field of view); 6, severe injury (up to 75% injury of the field of view); and 8, extremely severe injury (diffused injury) (10). The upper right lung lobes were excised and weighed to determine the wet/dry (W/D) ratio by comparing fresh weight to weight after 72 h of desiccation at 60˚C. Remaining lung tissues were quickly frozen in liquid nitrogen and maintained at -80˚C for future protein semi-quantification through ELISA and western blotting. This comprehensive sample collection and processing protocol enabled systematic evaluation of physiological parameters, histopathological changes, and molecular markers through techniques including ELISA, western blotting, RT-qPCR, and immunohistochemical (IHC) analysis using commercial assay kits, thereby providing a multi-faceted assessment of the ARDS model.

In the survival study (n=9 per group), mice received the following treatments: The ARDS model was induced by a single i.p. injection of LPS (10 mg/kg). After 30 min, the CA group received CA (40 mg/kg, i.p.), while the CA + ML385 group received ML385 (30 mg/kg, i.p.) followed by CA (40 mg/kg, i.p.), as previously described (23).Survival rates were recorded every 24 h for a 7-day observation period following LPS challenge and euthanized at the moribund stage. The humane endpoints were defined as the occurrence of moribund animal characteristics in the mice, such as severe or persistent lethargy, inability to rise from a recumbent position, convulsions, tetraplegia and dyspnea (24,25). Mortality was assessed through twice-daily monitoring (morning and evening) to ensure accurate determination of survival time points.

Cell culture. MH-S cells (murine alveolar macrophage cells) were obtained from The Cell Bank of Type Culture Collection of The Chinese Academy of Sciences. Cells were maintained in a culture medium consisting of DMEM, supplemented with 10% FBS and 1% penicillin and streptomycin. The cells were incubated at 37˚C in an environment containing 5% CO_2. Following the respective treatments, cell culture supernatants were collected for subsequent analysis by centrifugation of the culture medium at 1,000 x g for 5 min at 4˚C to remove cellular debris.

For *in vitro* investigations, MH-S cells were systematically allocated into the following four groups: i) Control group; ii) LPS/ATP group; iii) CA-10 group; and iv) CA-20 group. MH-S cells in the LPS/ATP, CA-10 and CA-20 groups were initially exposed to LPS (1 μg/ml) for 4 h at 37˚C, followed by ATP stimulation (5 mM) for 30 min at 37˚C (26). Subsequently, the CA-10 and CA-20 groups received either 10 or 20 μM CA and were further incubated for 48 h at 37˚C, whereas the control groups received equivalent volumes of culture medium.

Cell viability assay. A Cell Counting Kit-8 (CCK-8) assay was used to assess cell viability according to the instructions of the manufacturer. MH-S cells were plated in 96-well plates at a concentration of $5x10^3$ cells/well and left to adhere for 24 h under standard culture conditions. The cells were then exposed to CA (0, 0.1, 1, 10, 15, 20, 25, 30 and 35 μM) for 48 h at 37˚C. After treatment, each well received 10 μl CCK-8 solution (5 mg/ml) and the plates were incubated for 1 h at 37˚C in an environment with 5% CO_2. Absorbance was read at 450 nm

Table II. Primer sequences.

Gene	Forward primer	Reverse primer
NLRP3	5'-GCTGCGATCAACAGGCGAGAC-3'	5'-AAGGCTGTCCTCCTGGCATACC-3'
ASC	5'-AACCCAAGCAAGATGCGGAAG-3'	5'-TTAGGGCCTGGAGGAGCAAG-3'
CASP1	5'-ACAACCACTCGTACACGTCTTGC-3'	5'-CCAGATCCTCCAGCAGCAACTTC-3'
GSDMD	5'-ACTGAGGTCCACAGCCAAGAGG-3'	5'-GCCACTCGGAATGCCAGGATG-3'
Nrf2	5'-TCTCCTCGCTGGAAAAAGAA-3'	5'-AATGTGCTGGCTGTGCTTTA-3'
HO-1	5'-CAAGCCGAGAATGCTGAGTTCATG-3'	5'-GCAAGGGATGATTTCCTGCCAG-3'
GAPDH	5'-GCACCGTCAAGGCTGAGAAC-3'	5'-TGGTGAAGACGCCAGTGGA-3'

NLRP3, NLR family pyrin domain containing 3; ASC, apoptosis-associated speck-like protein containing a CARD; CASP1, caspase-1; GSDMD, gasdermin D; Nrf2, nuclear factor erythroid 2-related factor 2; HO-1, heme oxygenase-1.

with the model 680 microplate reader (Bio-Rad Laboratories, Inc.).

Reverse transcription-quantitative PCR (RT-qPCR) analysis. In accordance with a previous study (23), total RNA was extracted from lung tissues and cultured cells using TRIzol® reagent (Invitrogen; Thermo Fisher Scientific, Inc.), strictly adhering to the guidelines of the manufacturer. Subsequently, cDNA synthesis was performed using the RT Kit (Vazyme Biotech Co., Ltd.) according to the manufacturer's protocol. The qPCR amplification was then conducted on the SmartCycler® II system (Cepheid) using the following thermocycling conditions: Initial denaturation at 95˚C for 30 sec, followed by 40 cycles of denaturation at 95˚C for 10 sec and annealing/extension at 60˚C for 30 sec. A melting curve analysis was performed immediately after amplification to verify the specificity of the PCR products. GAPDH as the endogenous control. Relative gene expression levels were calculated using the $2^{-\Delta\Delta Cq}$ method (27). The specificity of the PCR amplification was confirmed by a single peak in the melting curve analysis. The primer sequences used are listed in Table II.

Western blotting. Protein lysates were prepared from both treated MH-S cells and mouse lung tissues using RIPA buffer supplemented with protease and phosphatase inhibitors. Protein concentrations were evaluated through the BCA assay kit, according to the manufacturer's protocol. Prior to electrophoresis, protein samples were mixed with 5X Laemmli sample buffer containing 5% β-mercaptoethanol (or 100 mM DTT) as a reducing agent and denatured by boiling at 95-100˚C for 5-10 min. For western blotting, protein lysates were adjusted to a concentration of 0.75 μg/μl for lung tissues or 1.0 μg/μl for MH-S cells using RIPA buffer. A total of 15 μg protein/lane was loaded for all samples, corresponding to 20 μl for lung tissues and 15 μl for cell lysates. Proteins were then separated by SDS-PAGE on 8-12% gels (depending on target protein size) under reducing conditions. The resolved proteins were then electrophoretically transferred onto PVDF membranes (0.45-μm pore size; MilliporeSigma) using a semi-dry transfer system.

Each target protein and its loading control, GAPDH, were ultimately detected on the same physical membrane to ensure direct comparability. This was achieved through sequential detection (stripping and re-probing) on a single membrane: For analysis of the inflammasome pathway, the membrane was first probed for NLRP3, ASC, and caspase-1 (p20). After imaging, the antibodies were stripped, and the same membrane was then re-probed for GAPDH. For analysis of GSDMD cleavage, the membrane was first probed for GSDMD-FL and GSDMD-N. After imaging, the antibodies were stripped, and the same membrane was then re-probed for GAPDH. Electrophoresis conditions were optimized to ensure sufficient separation between the GAPDH (~36 kDa) and GSDMD-N (30-35 kDa) bands prior to stripping and re-probing, allowing for accurate post hoc alignment and densitometric analysis.

Following transfer, all membranes were stained with Ponceau S to confirm uniform protein loading and transfer efficiency. The membranes were then blocked with 5% skimmed milk in Tris-buffered saline containing 0.1% Tween-20 (TBST) at 4˚C overnight (or for 1 h at room temperature if applicable). After washing three times with TBST (10 min each), the membranes were incubated with corresponding HRP-conjugated secondary antibodies diluted in 5% skimmed milk/TBST for 1 h at room temperature. Immunoreactive bands were detected using the Enhanced ECL Kit (cat. no. P0018; Beyotime Biotechnology) according to the manufacturer's instructions, and visualized using a Tanon-5200 Imaging System (Tanon Science & Technology Co., Ltd.). Between probing cycles, the membranes were stripped using a mild stripping buffer. Complete removal of previous antibodies was verified by incubating the membrane with ECL substrate and confirming the absence of signal prior to the next round of antibody incubation. Densitometric analysis of the bands was performed using ImageJ software (V1.37; National Institutes of Health). The signal intensity of each target protein was normalized to that of GAPDH obtained from the same membrane lane.

Immunohistochemical (IHC) analysis. Firstly, lung tissue samples were preserved in 4% paraformaldehyde at 4˚C for 1 day, processed through a graded ethanol series and embedded in paraffin blocks. Serial sections (5 μm) were then cut using the RM2235 rotary microtome (Leica Biosystems). The staining procedure involved: i) Deparaffinization in xylene (three changes, 5 min each); ii) rehydration through a graded ethanol series (100-70%); iii) antigen retrieval in citrate buffer (pH 6.0) at 95˚C for 20 min; iv) endogenous peroxidase blocking with 3% H_2O_2 for 10 min at room temperature; and

v) non-specific site blocking with 5% goat serum for 30 min at room temperature.

Sections were incubated with a primary antibody against gasdermin D (GSDMD; 1:1,000) overnight at 4˚C in a humidified environment. After three washes with PBS (5 min each), the sections were exposed to an HRP-conjugated secondary antibody (1:200) for 20 min at room temperature, followed by 3,3'-diaminobenzidine chromogen development (6 min) with microscopic monitoring. Counterstaining was performed with hematoxylin at room temperature for 30 sec, followed by dehydration through graded ethanol and xylene clearing. Slides were examined under the LSM700 confocal microscope (Zeiss GmbH). Semi-quantitative analysis of IHC staining was performed using ImageJ software.

For the co-detection of GSDMD-FL and GSDMD-N, the same membrane was used. Due to the close molecular weights of GSDMD-N and GAPDH, which could lead to overlapping bands and imprecise semi-quantification, GAPDH was probed on a separate membrane. Similarly, other target proteins (NLRP3, caspase-1 and ASC) were detected on dedicated membranes to optimize antibody conditions and avoid excessive stripping/re-probing cycles. To ensure perfect comparability between different membranes, total protein lysates for all samples were run on two identical SDS-PAGE gels in parallel under the same electrophoretic conditions. Proteins were then transferred in parallel onto separate PVDF membranes under identical transfer conditions. To control for loading and transfer variations, the membranes were stained with Ponceau S (Sigma-Aldrich) after transfer. Densitometric analysis of the total protein stain (Ponceau S) for each lane was performed using ImageJ software, and the signal intensity of each target protein was normalized to the total protein signal of its corresponding lane.

Immunofluorescence analysis. Cells were rinsed with PBS, fixed with 4% paraformaldehyde for 10 min at room temperature and then washed three times with TBST (5 min each). Permeabilization with 0.1% Triton X for 20 min at room temperature was carried out after another three TBST washes (5 min each). Primary antibodies of Nrf2 (as aforementioned) diluted in blocking buffer were then applied and incubated overnight at 4˚C in a humidified chamber. Subsequently, the cells were washed, incubated with secondary antibody for 1 h in the dark at room temperature and rinsed three times with TBST. Each sample received 200 μl antifade mounting medium with DAPI and visualization was performed using the LSM700 confocal microscope. Semi-quantitative analysis of IF staining was performed using ImageJ software.

ELISA. Concentrations of IL-1β and IL-18 in MH-S cell culture supernatants and BALF were quantified using ELISA kits following the manufacturer's protocols. Standards and samples (100 μl/well) were loaded in duplicate onto 96-well plates and incubated at 37˚C for 90 min. After washing, 100 μl biotinylated detection antibody was added to each well and incubated for 60 min at 37˚C. After three washes, 100 μl HRP-conjugated streptavidin was added and incubated for 30 min at 37˚C in the dark. The enzymatic reaction was terminated by adding 50 μl stop solution and the absorbance was immediately measured at 450 nm (with 570 nm correction) using the Bio-Rad Model 680 microplate reader (Bio-Rad Laboratories, Inc.). Cytokine concentrations were interpolated from a four-parameter logistic standard curve generated with reference standards.

Annexin V-FITC staining. MH-S cells were cultured in a 24-well plate. After treatment, the plates were centrifuged at 1,000 x g for 5 min at room temperature, the supernatant was removed and the cells were washed twice with PBS. Subsequently, the cells were stained with 250 μl Annexin V-FITC/PI solution for 15 min at room temperature in the dark. Images were then acquired using an IX73 inverted fluorescence microscope (Olympus Corporation).

Lactate dehydrogenase (LDH) release assay. Cytotoxicity was assessed by quantifying LDH activity in cell culture supernatants and BALF using a commercial LDH detection kit assay, following the product description. A total of 100 μl cell-free supernatant from each sample was transferred to a 96-well plate and incubated with the reaction mixture for 30 min at room temperature in the dark. The enzymatic reaction was terminated by adding stop solution and absorbance was immediately measured at 450 nm using the model 680 microplate reader (Bio-Rad Laboratories, Inc.).

Assessment of intracellular reactive oxygen species (ROS) levels. Intracellular ROS levels were quantified using 2',7'-dichlorodihydrofluorescein diacetate (DCFH-DA) as a fluorescent probe. Cells were seeded in 24-well plates ($5x10^4$ cells/well) and treated as indicated for 48 h at 37˚C. Subsequently, the cells were incubated with 10 μM DCFH-DA in serum-free medium at 37˚C for 20 min in the dark. After three washes with warm DMEM to remove excess probe, ROS detection was carried out using the IX73 inverted fluorescence microscope (Olympus Corporation).

Measurement of oxidative stress markers. Myeloperoxidase (MPO), malondialdehyde (MDA) and superoxide dismutase (SOD) oxidative stress marker activity was quantitatively analyzed in both cell culture supernatants and BALF using commercial assay kits according to the manufacturer's protocols. All spectrophotometric measurements were carried out in triplicate using the model 680 microplate reader (Bio-Rad Laboratories, Inc.), with appropriate blank and standard controls included in each assay plate.

Statistical analysis. All quantitative data, except for survival data, are presented as the mean ± standard deviation (SD) from at least three independent experiments, with each experiment carried out in triplicate. Statistical analyses were carried out using GraphPad Prism (version 6.0; Dotmatics). For comparisons between multiple groups, one-way analysis of variance (ANOVA) was performed: for data with homogeneous variances, Tukey's post hoc test was used; for data with heterogeneous variances, Welch's ANOVA followed by Games-Howell's post hoc test was employed. For the survival study, Kaplan-Meier survival curves were generated, and differences between groups were compared for statistical significance using the log-rank (Mantel-Cox) test. In all analyses, a P-value of less than 0.05 ($P<0.05$) was considered to indicate a statistically significant difference.

Results

Network pharmacology analysis

Target screening of CA and ARDS. The two-dimensional structure of CA was retrieved from the PubChem

database (Fig. 1A). Target prediction analysis using the SwissTargetPrediction platform identified 106 potential CA target genes (probability score, >0.1). In addition, 496 ARDS-associated genes were compiled from comprehensive disease databases (GeneCards, 387 targets; DisGeNET, 109 targets) after removing duplicates. Comparative analysis through a Venn diagram revealed 19 overlapping genes between CA targets and ARDS-related genes (Fig. 1B), representing potential therapeutic targets through which CA may exert its pharmacological effects against ARDS. These 19 candidate targets were subsequently prioritized for further network pharmacology analysis.

Functional enrichment analysis. Bioinformatics analysis using the Metascape platform revealed significant functional enrichment among the 19 common targets, identifying 466 GO BP, 22 GO CC, 56 GO MF and 37 KEGG pathways. BP analysis demonstrated that these targets were predominantly involved in 'regulation of reactive oxygen species metabolic process' (GO: 2000377), 'positive regulation of cell death', 'regulation of apoptotic signaling pathway' and 'regulation of DNA-binding transcription factor activity', suggesting these BP may mediate the therapeutic effects of CA in ARDS (Fig. 1C). MF analysis results demonstrated that the common target genes were most involved in 'metallopeptidase activity', 'serine-type peptidase activity' and 'serine hydrolase activity'. CC analysis results indicated that the common target genes were the most predicated on the 'extracellular matrix', 'external encapsulating structure' and 'tertiary granule'. Results of the KEGG analysis revealed that the 19 genes were mainly enriched in 'Fluid shear stress and atherosclerosis', 'Pathways in cancer', 'Lipid and atherosclerosis' and the 'IL-17 signaling pathway' (Fig. 1D).

PPI network construction. Among the 19 genes, ADCY10 was excluded from PPI network construction as it exhibited no association with the other genes. The finalized network comprised 18 nodes and 80 edges, illustrating the complex web of interactions among the remaining targets (Fig. 1E). Hub targets were subsequently identified to uncover the core characteristics of the network. These key nodes were pinpointed based on their degree values, which effectively captured their relative importance and connectivity within the network, providing insight into the functional architecture of the network.

Molecular docking and MD. Following comprehensive analysis of the PPI network, NFE2L2 (encoding the Nrf2 protein) emerged as the pivotal target. Subsequently, to explore the potential binding mode and interaction mechanism, molecular docking experiments were conducted between NFE2L2 and CA. A total of 10 different docking sites were assessed, with findings indicating that the docking affinity was <-5 kcal/mol (Table III). Subsequently, the top-ranked conformation from the molecular docking results, which demonstrated the highest binding affinity, was subjected to MD simulations for further validation. All results suggested that NFE2L2 and CA are capable of stable binding (Fig. 2). As shown in Fig. 2A-C, the RMSD of the complex, protein and ligand CA, the radius of gyration, and the root-mean-square fluctuation of amino acid residues all stabilized over the 100 nsec molecular dynamics simulation, indicating that the complex system reached equilibrium and the binding conformation remained stable. Further binding analysis revealed that the distance between CA and the Nrf2 binding site, as well as the buried solvent-accessible surface area, remained stable during the later stages of the simulation (Fig. 2D-E). Moreover, superimposed simulation conformations demonstrated that CA stably bound the initial docking site (Fig. 2F). Binding free energy calculations (molecular mechanics Poisson-Boltzmann surface area) revealed that van der Waals interactions served as the primary driving force for binding. Additionally, residual energy decomposition analysis identified key amino acids, such as GLY-464 and VAL-463, that contributed significantly to the binding energy (Fig. 2H). These results confirm at the atomic level that CA and Nrf2 can form a stable complex, providing a theoretical foundation for subsequent experimental validation.

Table III. Molecular docking affinity between carnosic acid and the target protein nuclear factor erythroid 2-related factor 2.

Dock poses	Affinity, kcal/mol	RMSD l.b.	RMSD u.b.
1	-9.606	0	0
2	-9.508	1.605	6.209
3	-9.473	1.861	6.457
4	-8.859	4.454	7.007
5	-8.743	4.177	6.832
6	-8.615	4.637	7.487
7	-8.588	3.847	6.335
8	-8.396	2.010	3.009
9	-8.266	1.572	2.136
10	-7.930	6.649	10.900

RMSD, root mean square deviation; l.b., lower bound; u.b., upper bound.

Biological experiment results

Effect of CA on MH-S cell viability. A CCK-8 assay was used to assess the cytotoxic effects of CA on MH-S cells. The results demonstrated that low CA concentrations (1-20 μM) did not significantly affect cell viability. Based on these findings, 10 and 20 μM CA concentrations were selected for subsequent experimental investigation (Fig. 3A).

CA inhibits pyroptosis in LPS/ATP-stimulated MH-S cells. To assess the impact of CA on pyroptosis, MH-S cells were treated with LPS and ATP. Pyroptosis was then quantified by measuring the proportion of PI-positive cells (Annexin V-FITC and PI double staining, a combination of methods evaluating membrane integrity and inflammasome activation) and LDH levels in the cell supernatant. The findings indicated a notable reduction in both LDH release (Fig. 3B) and PI-positive cells (Fig. 3C and D) following CA treatment. During the early stages of apoptosis and pyroptosis, phosphatidylserine becomes externalized on the cell membrane. However, pyroptosis ultimately leads to complete membrane rupture. Consequently, a cell population positive for Annexin V-FITC (green) and negative for PI (red) indicates an early stage of cell death, while cells positive for both Annexin V and PI represent a later stage characterized by loss of membrane

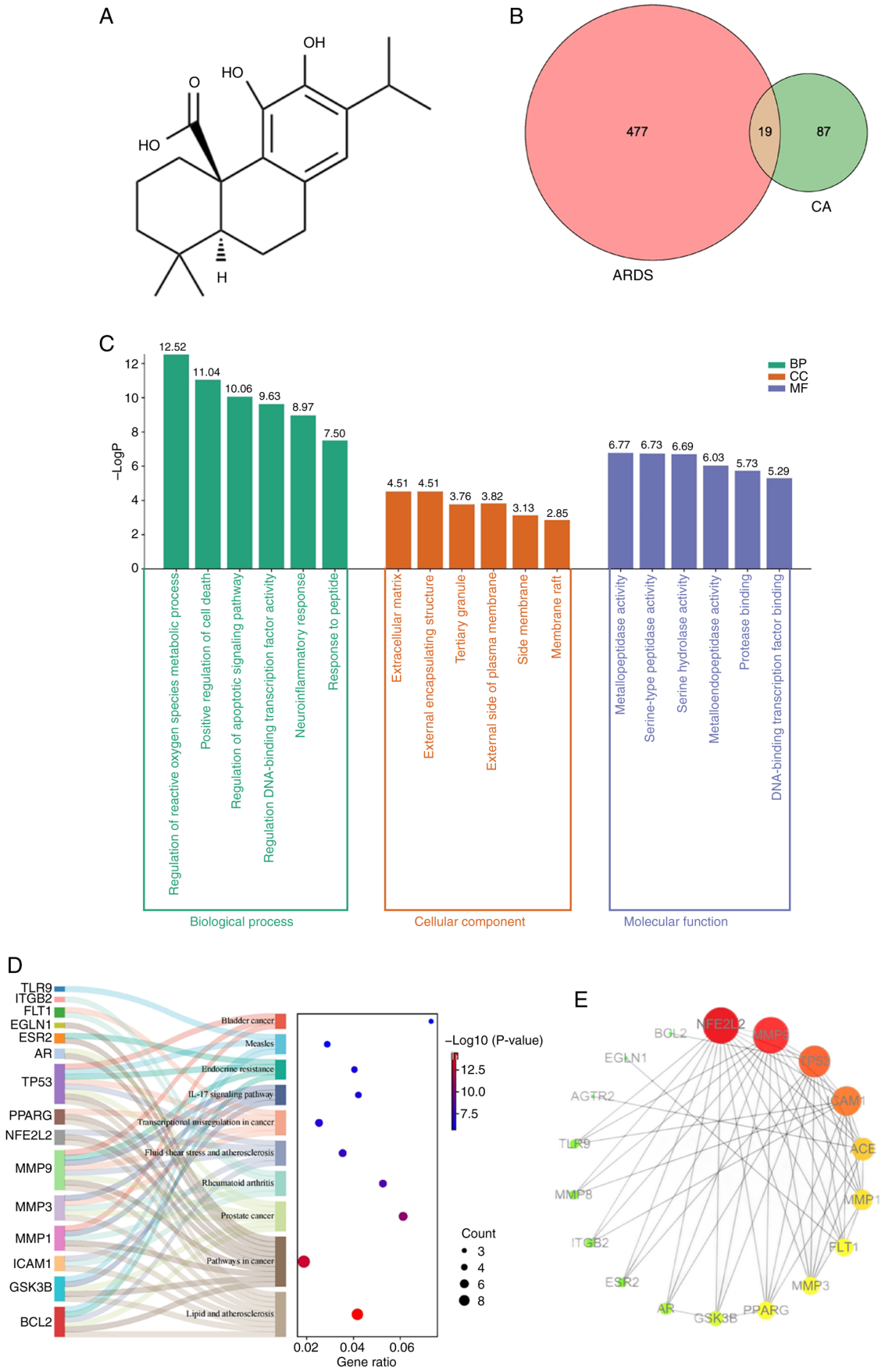

Figure 1. Network pharmacological analysis of CA on ARDS. (A) Two-dimensional structure of CA retrieved from the PubChem database. (B) Venn diagram exhibiting common targets between CA and ARDS. (C) Functional enrichment analysis of target genes through Gene Ontology analysis, encompassing BP, CC and MF. (D) Kyoto Encyclopedia of Genes and Genomes pathway analysis of target genes. (E) Protein-protein interaction network diagram of overlapping target genes. In the PPI network, individual nodes symbolize proteins, while the connecting edges represent the relationships between these proteins. CA, carnosic acid; ARDS, acute respiratory distress syndrome; BP, biological processes; MF, molecular functions; CC, cellular components.

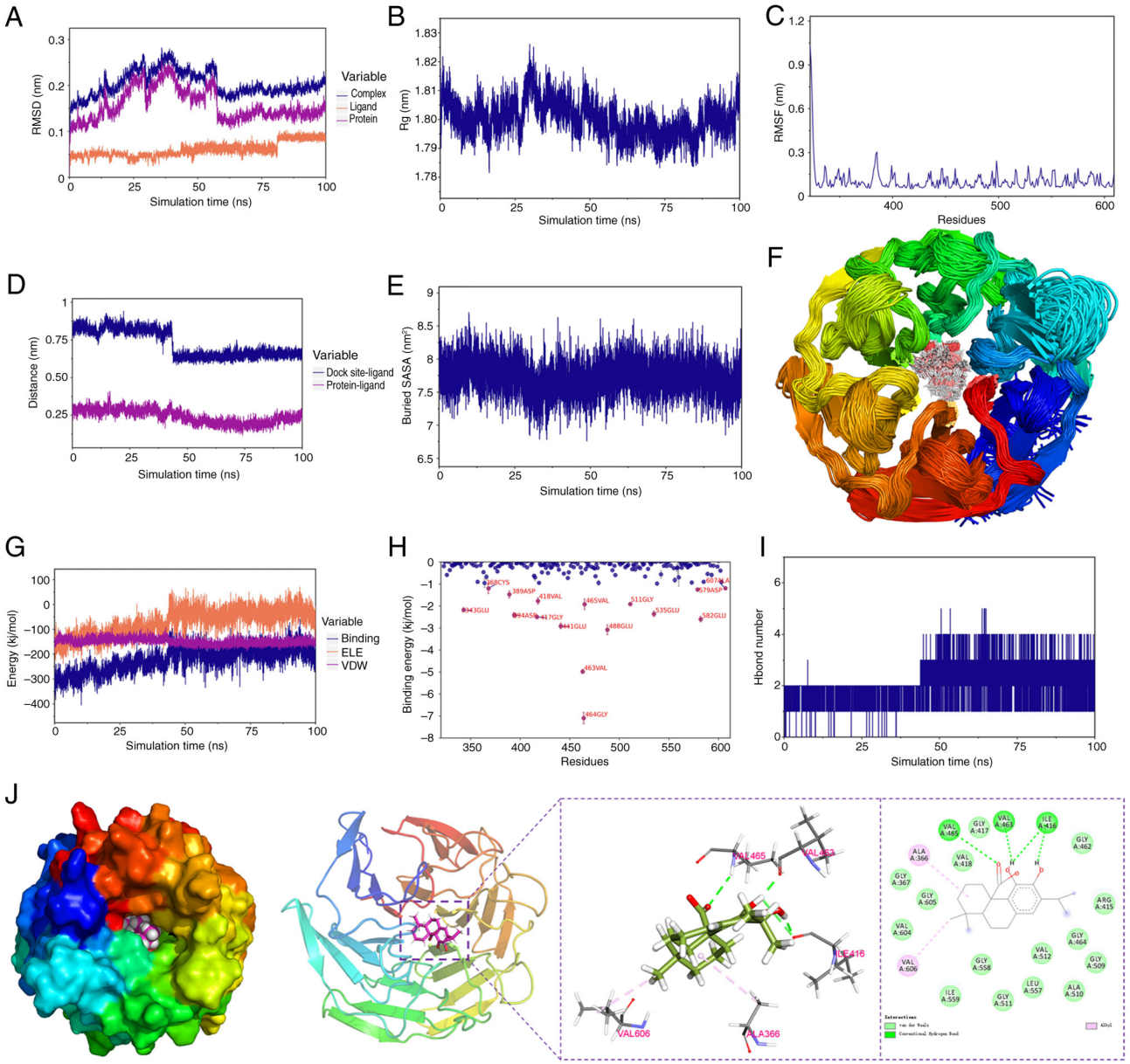

Figure 2. Molecular docking and molecular dynamics simulation of CA and Nrf2. (A) RMSD calculation of the complex. (B) Rg of the complex. (C) RMSF calculation of the protein in the complex. (D) Distance between the docking site of the protein and the small molecule ligand (dock site-ligand). (E) Buried SASA between the small molecule and the protein. (F) Superposition of the simulated conformations. (G) VDW and ELE binding energies between the small molecule and the protein. (H) Contribution of amino acid binding energy. (I) Hbond number. (J) Interaction between the protein and the small molecule. RMSD, root mean square deviation; Rg, radius of gyration; RMSF, root mean square fluctuation; SASA, solvent-accessible surface area; ELE, electrostatic energy; VDW, van der Waals.

integrity. The results demonstrated that LPS/ATP stimulation significantly increased the proportion of double-positive cells, an effect that was effectively reversed by CA treatment. To assess NLR family pyrin domain containing 3 (NLRP3) inflammasome activation, key markers were examined, including apoptosis-associated speck-like protein containing a CARD (ASC), caspase-1 (CASP1), the N-terminal fragment of GSDMD and the downstream cytokines IL-18 and IL-1β. CA treatment significantly inhibited the protein expression of these key markers induced by LPS/ATP and their corresponding mRNA upregulation (Fig. 3E-G). Furthermore, CA markedly attenuated the release of IL-18 and IL-1β in the supernatant compared with the LPS/ATP-stimulated group (Fig. 3H). Collectively, these outcomes indicated that CA may effectively hinder LPS/ATP-induced pyroptosis in MH-S cells by inhibiting NLRP3 activation and averting GSDMD cleavage.

CA activates Nrf2 and alleviates oxidative stress in LPS/ATP-stimulated MH-S cells. CA has previously been documented to exhibit potent antioxidative properties (28); however, its protective effects against oxidative stress in MH-S cells remain unclear. Thus, the antioxidant effects and underlying mechanisms of CA in LPS/ATP-challenged MH-S cells were investigated.

To assess the antioxidant properties of CA, the key oxidative stress markers MDA, MPO and SOD were analyzed. CA treatment significantly reduced MDA and MPO levels while enhancing SOD activity in MH-S cells compared with the

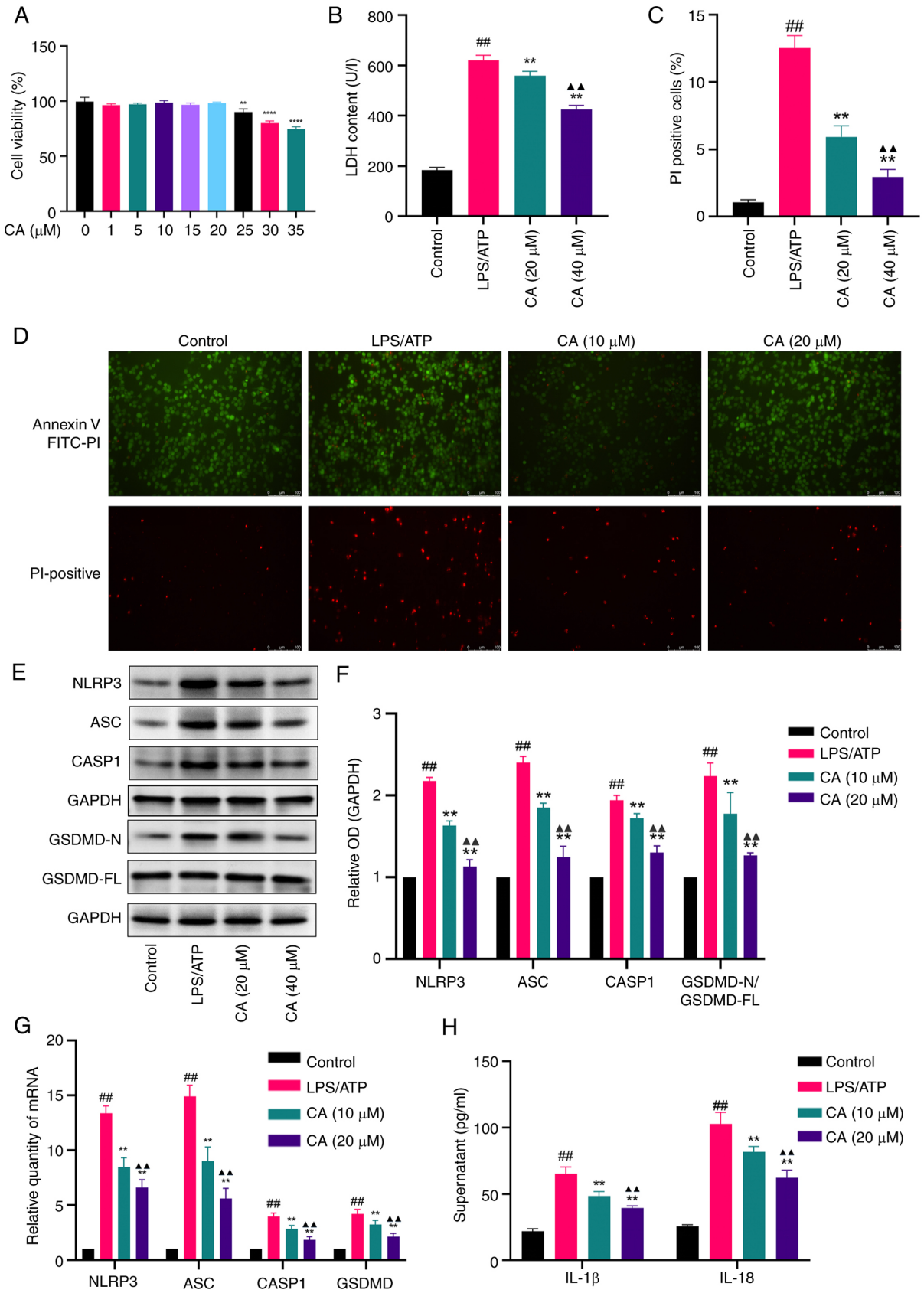

Figure 3. CA inhibits pyroptosis in LPS/ATP-stimulated MH-S cells. (A) Cytotoxicity of CA evaluated by a Cell Counting Kit-8 assay. (B) LDH release in the supernatant following CA treatment. (C) Percentage of PI-positive cells following CA treatment. (D) Annexin V-FITC (green) double-fluorescent staining representing apoptosis levels and PI (red) double-fluorescent staining representing cell necrosis levels. Scale bar, 100 μm. PI-positive cell rate was calculated using ImageJ software. (E) Representative bands and (F) analysis of protein expression of NLRP3, ASC, CASP1 and GSDMD detected by western blotting. (G) mRNA expression levels of NLRP3, ASC, CASP1 and GSDMD detected by reverse transcription-quantitative PCR. (H) Production of IL-18 and IL-1β in the supernatant measured by ELISA. Data are presented as the mean ± SD of three independent experiments. $^{\#\#}$P<0.01 vs. control; **P<0.01, ****P<0.0001 vs. LPS/ATP; $^{\blacktriangle\blacktriangle}$P<0.01 vs. CA (10 μM). CA, carnosic acid; LPS, lipopolysaccharide; LDH, lactate dehydrogenase; NLRP3, NLR family pyrin domain containing 3; ASC, apoptosis-associated speck-like protein containing a CARD; CASP1, caspase-1; GSDMD, gasdermin D; OD, optical density.

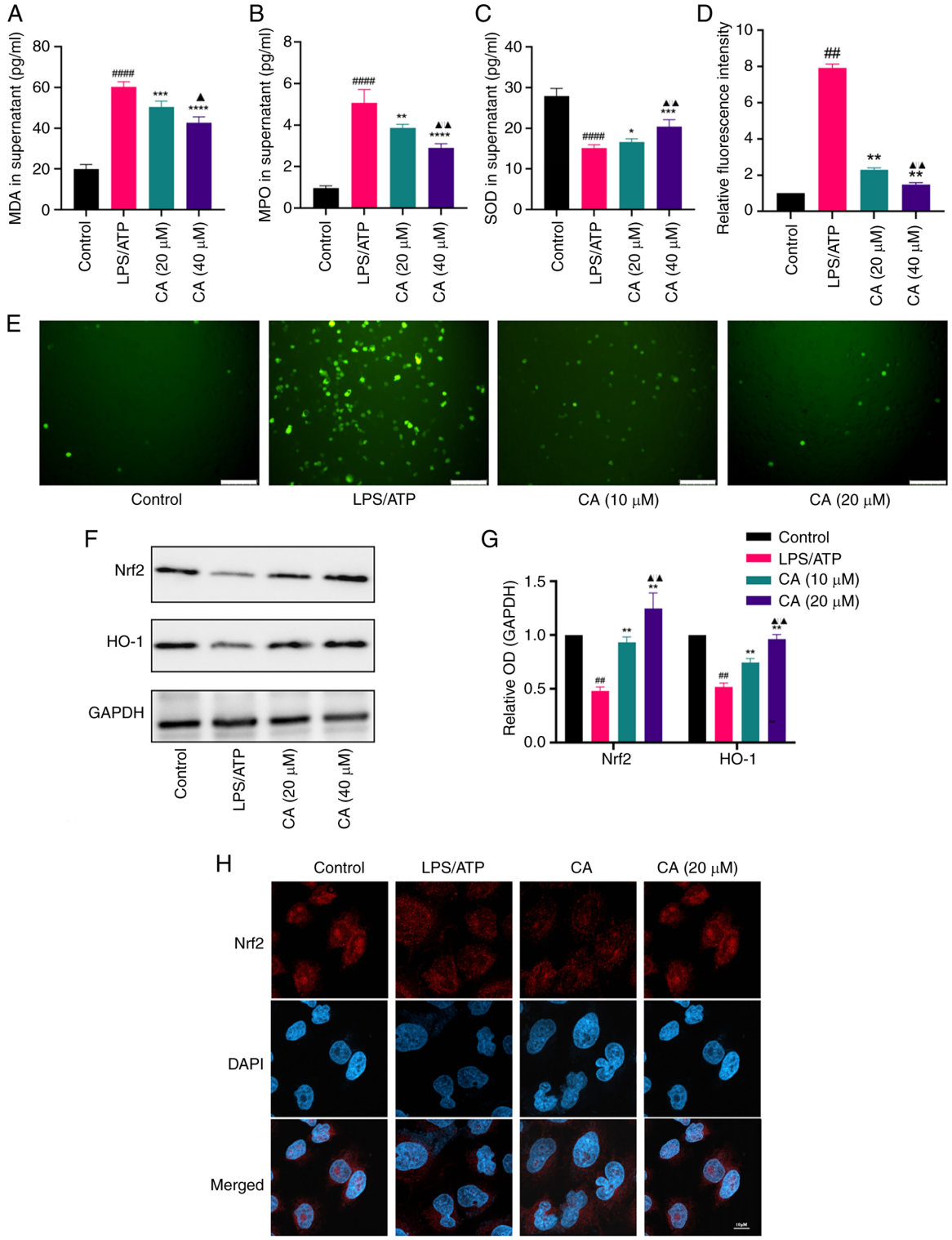

Figure 4. CA activates Nrf2 and improves the oxidative stress in LPS/ATP-stimulated MH-S cells. Levels of (A) MDA, (B) MPO and (C) SOD in the supernatant measured by ELISA. (D and E) ROS generation of MH-S cells detected by 2',7'-dichlorodihydrofluorescein diacetate cellular ROS detection assay, with fluorescence intensity calculated using ImageJ software. Scale bar, 100 μm. (F) Representative bands and (G) analysis of protein expression of Nrf2 and HO-1 detected by western blotting. (H) Nuclear translocation of the Nrf2 subunit determined by an immunofluorescence assay. Scale bar, 20 μm. Data are presented as the mean ± SD of three independent experiments. $^{\#\#}$P<0.01, $^{\#\#\#\#}$P<0.0001 vs. control; *P<0.05, **P<0.01, ***P<0.001, ****P<0.0001 vs. LPS/ATP group; $^{\blacktriangle}$P<0.05, $^{\blacktriangle\blacktriangle}$P<0.01 vs. CA (10 μM). CA, carnosic acid; Nrf2, nuclear factor erythroid 2-related factor 2; HO-1, heme oxygenase-1; LPS, lipopolysaccharide; MDA, malondialdehyde; MPO, myeloperoxidase; SOD, superoxide dismutase; ROS, reactive oxygen species; OD, optical density.

LPS/ATP group (Fig. 4A-C). In addition, LPS/ATP stimulation led to a notable increase in intracellular ROS production in MH-S cells compared with that in the control group, with CA treatment effectively mitigating this increase (Fig. 4D and E).

Subsequently, the molecular mechanisms responsible for the antioxidant properties of CA were explored. Nrf2, a regulator of cellular antioxidant responses, was focused on to determine its involvement in CA-mediated oxidative stress protection (29). The

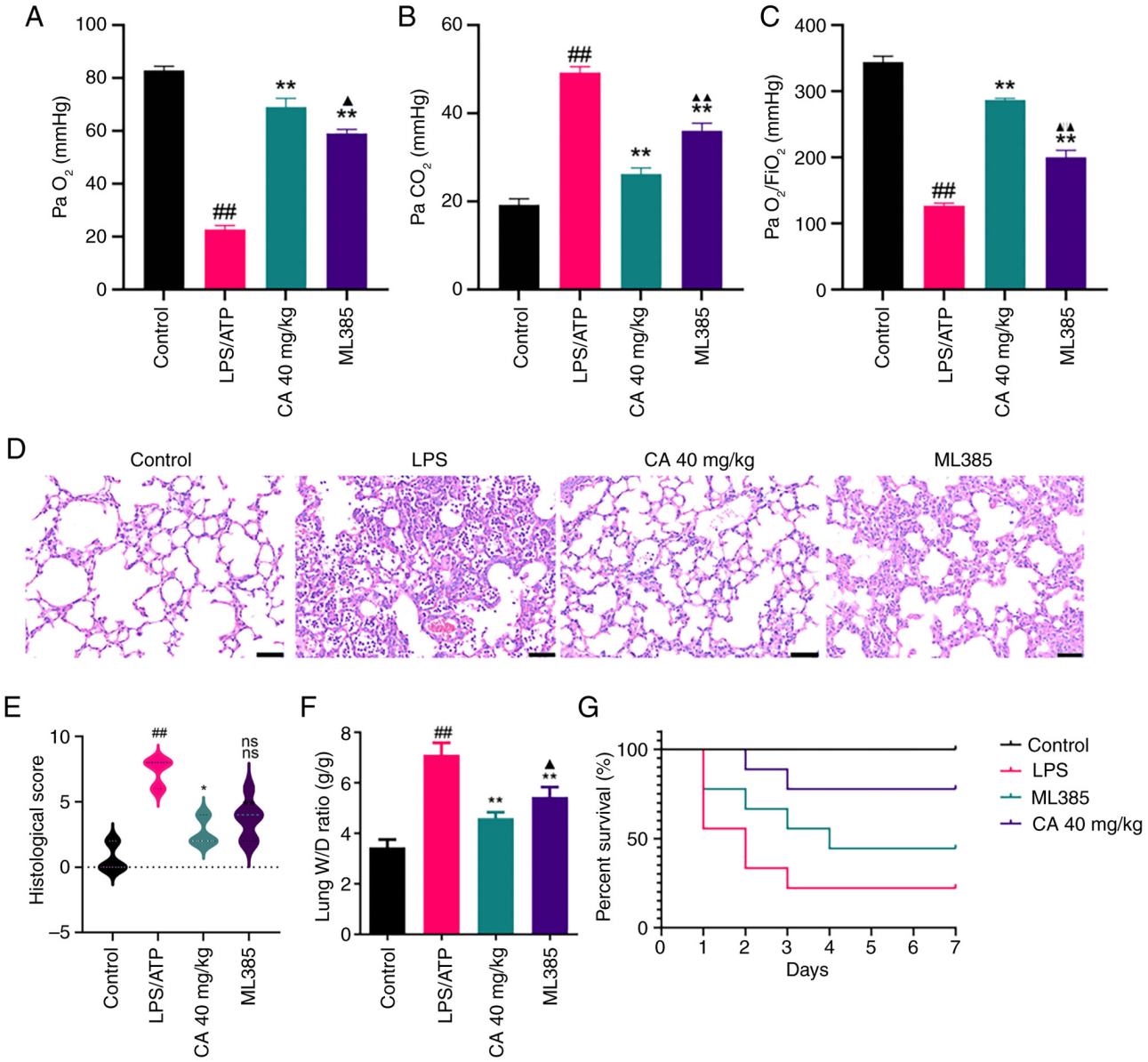

Figure 5. CA attenuates LPS-induced acute respiratory distress syndrome in mice. (A) PaO_2 and (B) $PaCO_2$ data of each group. (C) PaO_2/FiO_2 ratio of each group. (D) Histopathological variation in lung tissues determined using H&E staining. Scale bar, 50 μm. (E) Lung injury score. (F) Lung W/D ratio assessed using histological sections. (G) Survival rate for mice observed twice daily for 7 days. Data are presented as the mean ± SD of three independent experiments. $^{\#\#}$P<0.01 vs. control; *P<0.05, **P<0.01 vs. LPS; $^{\blacktriangle}$P<0.05, $^{\blacktriangle\blacktriangle}$P<0.01 vs. CA (40 mg/kg). CA, carnosic acid; LPS, lipopolysaccharide; ns, not significant; PaO_2, partial pressure of oxygen; $PaCO_2$, partial pressure of carbon dioxide; FiO_2, fraction of inspired oxygen; W/D, wet dry.

findings demonstrated that, compared to the LPS/ATP-stimulated group, CA treatment significantly augmented the protein expression of both total Nrf2 and heme oxygenase-1 (Fig. 4F and G) and facilitated the nuclear translocation of Nrf2 (Fig. 4H). Collectively, these findings suggested that CA may alleviate oxidative stress and activate Nrf2 in MH-S cells.

CA attenuates LPS-induced ARDS in mice. Arterial blood gas analysis showed that, in comparison with the control group, the LPS group exhibited a notable decrease in PaO_2 and PO_2/FiO_2 levels, and a marked increase in $PaCO_2$ levels (Fig. 5A-C). These characteristic alterations in blood gas parameters confirm the successful establishment of the ARDS mouse model (23). The mice that received treatment with CA demonstrated an elevation in PaO_2 levels and a significant decrease in $PaCO_2$ levels, indicating a marked improvement in pulmonary gas exchange, thus supporting its potential for clinical application.

The effects of CA against LPS-induced ARDS were subsequently evaluated by performing histopathological analysis of lung tissues using H&E staining (Fig. 5D). Compared with in the control group, LPS-challenged mice exhibited significantly elevated histological scores, characterized by extensive inflammatory cell infiltration, alveolar hemorrhage and interstitial edema (Fig. 5E). Notably, CA treatment markedly attenuated these pathological alterations and significantly improved histological scores. These findings provide histological evidence for the protective role of CA in mitigating LPS-induced acute lung injury.

To further assess pulmonary edema formation, lung tissue water content was quantified by measuring the W/D

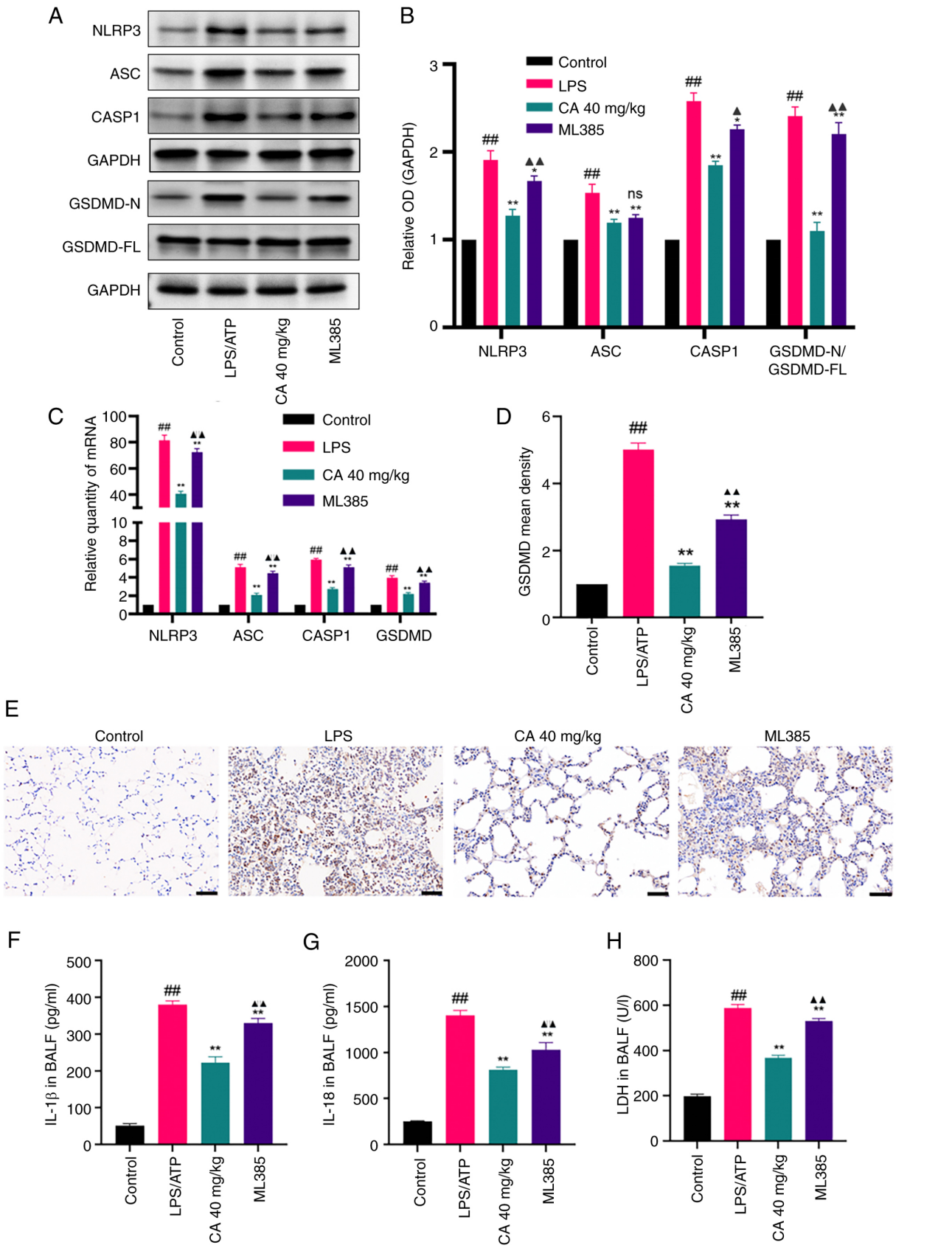

Figure 6. CA inhibits NLRP3 inflammasome-mediated pyroptosis in LPS-induced acute respiratory distress syndrome in mice. (A) Representative bands and (B) analysis of protein expression of NLRP3, ASC, CASP1 and GSDMD detected by western blotting. (C) mRNA expression levels of NLRP3, ASC, CASP1 and GSDMD detected by reverse transcription-quantitative PCR. (D) Analysis and (E) immunohistochemical staining showing the positive rate of GSDMD protein expression in lung tissues of mice in each group. Scale bar, 50 μm. Production of (F) IL-18 and (G) IL-1β in the BALF measured by ELISA. (H) LDH release in the BALF. Data are presented as the mean ± SD of three independent experiments. $^{\#\#}$P<0.01 vs. control; *P<0.05, **P<0.01 vs. LPS; $^{\blacktriangle}$P<0.05, $^{\blacktriangle\blacktriangle}$P<0.01 vs. CA (40 mg/kg). CA, carnosic acid; NLRP3, NLR family pyrin domain containing 3; LPS, lipopolysaccharide; ASC, apoptosis-associated speck-like protein containing a CARD; CASP1, caspase-1; GSDMD, gasdermin D; LDH, lactate dehydrogenase; BALF, bronchoalveolar lavage fluid; ns, not significant; OD, optical density.

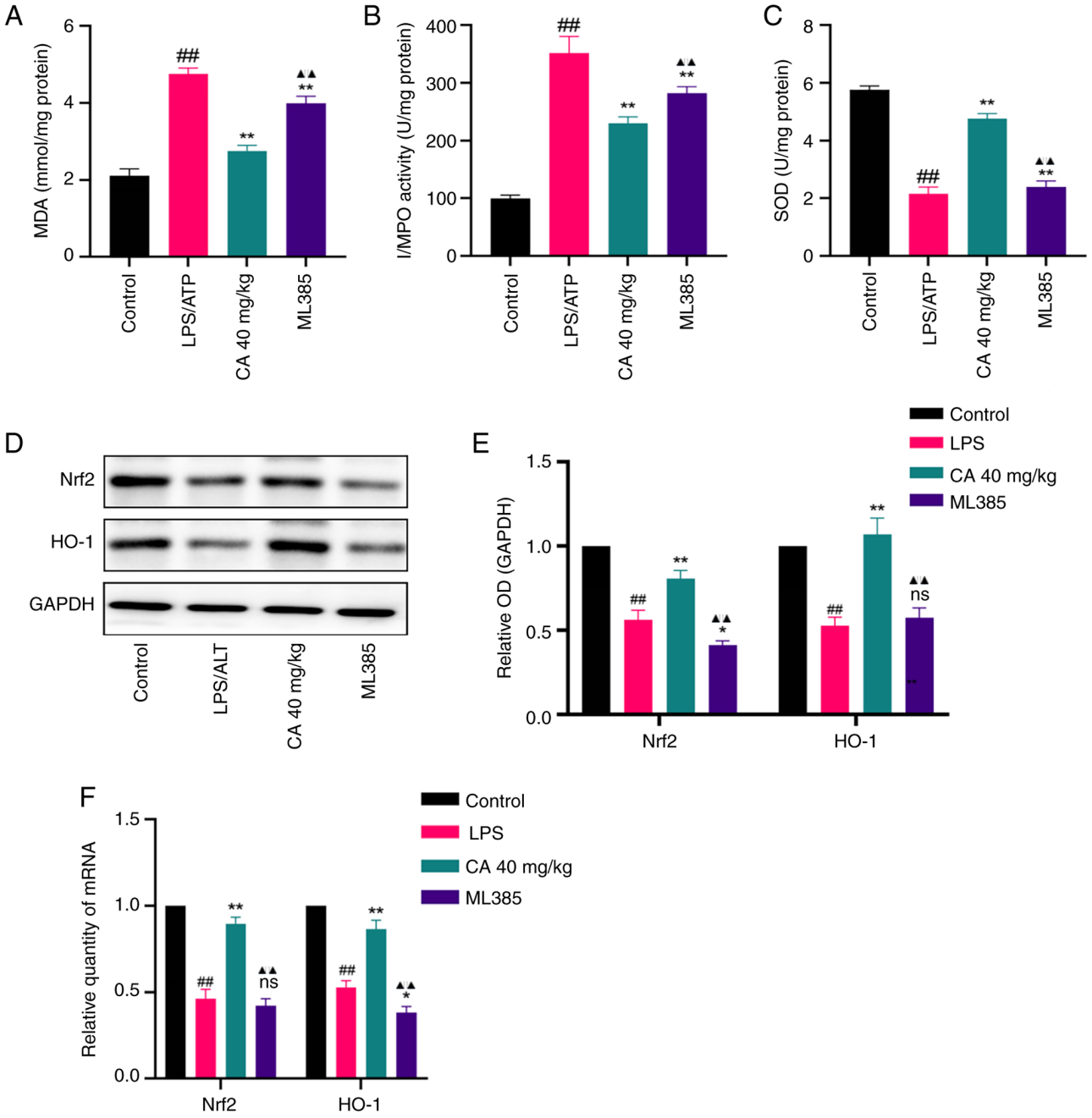

Figure 7. CA exerts an anti-oxidative effect in LPS-induced acute respiratory distress syndrome. Levels of (A) MDA, (B) MPO and (C) SOD in the bronchoalveolar lavage fluid measured by ELISA. (D) Representative bands and (E) analysis of protein expression of Nrf2 and HO-1 detected by western blotting. (F) mRNA expression of Nrf2 and HO-1 detected by reverse transcription-quantitative PCR. Data are presented as the mean ± SD of three independent experiments. $^{\#\#}$P<0.01 vs. control; *P<0.05, **P<0.01 vs. LPS; $^{\blacktriangle\blacktriangle}$P<0.01 vs. CA (40 mg/kg). CA, carnosic acid; LPS, lipopolysaccharide; MDA, malondialdehyde; MPO, myeloperoxidase; SOD, superoxide dismutase; Nrf2, nuclear factor erythroid 2-related factor 2; HO-1, heme oxygenase-1; ns, not significant; OD, optical density.

weight ratio. As shown in Fig. 5F, ARDS mice exhibited a significantly elevated lung W/D ratio compared with that in the control group, indicating severe pulmonary edema. Notably, CA treatment effectively normalized this parameter. Together with the histological findings, these results demonstrated that CA could confer marked protection against ARDS by attenuating pathological vascular permeability and edema formation.

Consistent with its reversal of CA-mediated improvements in lung injury parameters (Fig. 5A-F), pharmacological inhibition of Nrf2 with ML385 also significantly attenuated the survival benefit conferred by CA. Survival analysis via the Kaplan-Meier method revealed marked differences between groups (log-rank test, Fig. 5G). LPS-challenged mice only exhibited a 20% survival rate, treatment with CA markedly improved survival rates to >50%. Pharmacological inhibition of Nrf2 with ML385 attenuated the protective effects of CA, thus reducing survival rates. These findings suggested that CA may provide a notable survival benefit in LPS-induced ARDS, mediated through Nrf2 pathway activation.

CA inhibits NLRP3 inflammasome-mediated pyroptosis in mice with LPS-induced ARDS through activation of Nrf2. To

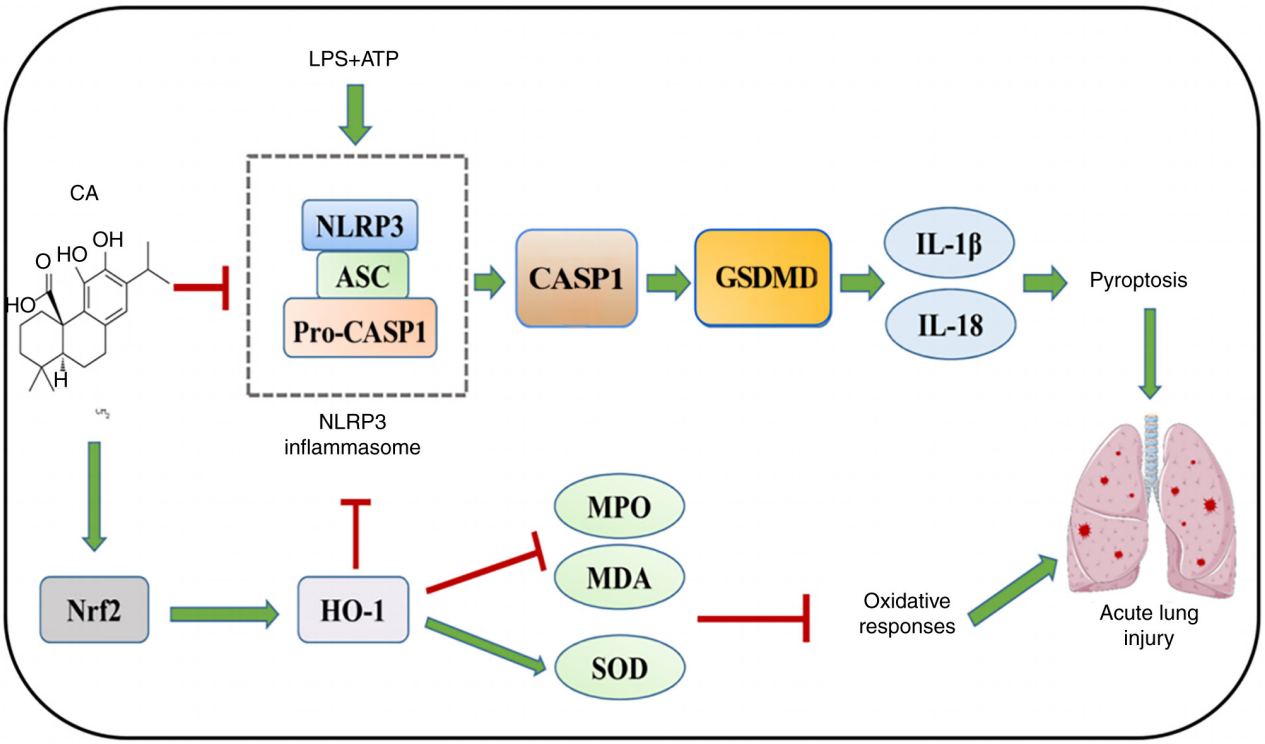

Figure 8. CA protects against acute respiratory distress syndrome by targeting Nrf2, suppressing oxidative stress and pyroptosis. LPS activates the NLRP3/CASP1/GSDMD signaling pathway to induce pyroptosis. CA inhibits oxidative stress and pyroptosis by activating Nrf2 to reduce lung injury. CA, carnosic acid; LPS, lipopolysaccharide; NLRP3, NLR family pyrin domain containing 3; ASC, apoptosis-associated speck-like protein containing a CARD; CASP1, caspase-1; HO-1, heme oxygenase-1, MPO, myeloperoxidase; MDA, malondialdehyde; SOD, superoxide dismutase; GSDMD, gasdermin D; Nrf2, nuclear factor erythroid 2-related factor 2.

further explore the anti-pyroptotic effect of CA and its protective role in LPS-induced ARDS, the impact of CA on NLRP3 inflammasome-mediated pyroptosis was investigated *in vivo*. Quantitative analysis revealed that LPS challenge induced pyroptotic activation, as evidenced by significant upregulation of NLRP3 inflammasome components (NLRP3, ASC, CASP1 and GSDMD) at both transcriptional and translational levels (Fig. 6A-E). This was associated with elevated BALF concentrations of pro-inflammatory cytokines IL-1β (Fig. 6F) and IL-18 (Fig. 6G), and increased LDH release (Fig. 6F). Notably, CA exerts its effects by selectively inhibiting the activation of the NLRP3 inflammasome, reducing LDH release and decreasing IL-18 and IL-1β secretion, thereby demonstrating the anti-pyroptotic effects observed *in vitro* through suppression of the NLRP3 inflammasome pathway.

To explore whether the effects of CA were Nrf2-dependent, mice were pretreated with the Nrf2 inhibitor ML385. This pretreatment eliminated the ability of CA to downregulate NLRP3 inflammasome components and reduce inflammatory mediator release (Fig. 6A-H). Therefore, these findings suggested that CA could attenuate LPS-induced ARDS by suppressing NLRP3 inflammasome-mediated pyroptosis, a process partially dependent on Nrf2 activation.

CA alleviates LPS-induced ARDS through Nrf2-dependent antioxidant mechanisms. MPO, MDA and SOD activity was assessed to evaluate whether CA exerted a protective effect against LPS-induced ARDS through its antioxidant properties. In addition, the protein and mRNA levels of Nrf2 and HO-1 were measured. The findings revealed that LPS administration notably elevated MPO and MDA activities, while suppressing SOD levels in the BALF (Fig. 7A-C). However, these changes were effectively prevented by pretreatment with CA. Additionally, treatment with CA resulted in a notable upregulation of both Nrf2 and HO-1 at both transcriptional and translational levels in the lung tissue of mice (Fig. 7D-F).

To further substantiate whether the antioxidant protection offered by CA against LPS-induced ARDS was dependent upon Nrf2 activation, mice were pretreated with the aforementioned ML385. ML385 not only abolished the CA-mediated reduction in MPO and MDA levels and the restoration of SOD activity (Fig. 7A-C), but also attenuated the CA-induced upregulation of both Nrf2 and HO-1 (Fig. 7D-F). These findings indicated that Nrf2 activation constitutes an essential mechanism underlying the antioxidant protection of CA in LPS-induced ARDS.

Discussion

ARDS is a severe respiratory disease marked by high rates of mortality (30-50%). To the best of our knowledge, at the present time, no treatment has been demonstrated as completely effective and conclusive for managing ARDS (2). As phytochemistry and pharmacological research have advanced, numerous natural products exhibiting antioxidant (30,31), anti-inflammatory (32,33) and antibacterial (34,35) properties have emerged. Consequently, there is a growing interest in utilizing the botanical constituents of traditional medicines as potential preventative

and therapeutic agents for ARDS (4,36). CA, a naturally occurring compound derived from *Rosmarinus officinalis* Linnaeus, has demonstrated promising antioxidant and anti-inflammatory effects (37,38). The present study systematically investigated the therapeutic potential and molecular mechanisms of CA against LPS-induced ARDS, employing an integrative approach combining network pharmacology, molecular docking, MD simulations, and comprehensive *in vitro* and *in vivo* validation experiments.

Network pharmacology identified 19 overlapping targets between CA and ARDS, with NFE2L2 (Nrf2) emerging as the hub target based on Venn and PPI network analysis. GO analysis suggested that the regulation of the ROS metabolic process is an important biological process in the mechanism of how CA treats ARDS. Research has suggested that uncontrolled oxidative stress markedly aggravates pulmonary inflammation, and accelerates the development and progression of ARDS (39,40). Central to this process is Nrf2, a key transcriptional factor that governs cellular antioxidant defense systems and maintains redox equilibria. Nrf2 activation induces the expression of cytoprotective enzymes, including HO-1, creating a key defense mechanism against oxidative damage. Emerging evidence has indicated that Nrf2/HO-1 pathway activation is specifically associated with ARDS mitigation through oxidative stress suppression (41,42). Building on these findings and considering the documented antioxidant properties of CA, it was hypothesized that CA could ameliorate LPS-induced ARDS through Nrf2/HO-1 pathway activation. Computational analyses, including molecular docking and MD simulations, demonstrated that CA forms stable binding complexes with the Nrf2 protein, perhaps indicating direct modulation of this transcriptional regulator. This prediction was experimentally validated in both cellular and animal models, whereby CA upregulated the protein and mRNA expression levels of Nrf2 and HO-1, decreased the levels of MPO and MDA, and increased the level of SOD. CA was also found to exert its antioxidant effects by reversing the LPS-induced downregulation of Nrf2, suggesting that CA serves an antioxidant role in LPS-induced ARDS through modulation of the Nrf2/HO-1 signaling pathway.

KEGG pathway enrichment analysis revealed that the most significantly enriched pathways were primarily associated with oxidative stress and inflammatory responses.. GO analysis suggested that the BP term 'positive regulation of cell death' is also important. Macrophages are important inflammatory response cells and there is increasing evidence suggesting that macrophages are involved in the pathogenesis of ARDS. Activated macrophages exacerbate pulmonary edema in LPS-induced ARDS through excessive production of pro-inflammatory mediators (43). Particularly, hyperactivation of the NLRP3 inflammasome has been shown to amplify lung inflammation and tissue injury (44). Mechanistically, NLRP3 inflammasome activation triggers CASP1-dependent cleavage of GSDMD, leading to the release of IL-1β and IL-18, which ultimately drives pyroptotic cell death. Despite these advances, the specific involvement of NLRP3 inflammasome-mediated macrophage pyroptosis in ARDS progression remains poorly characterized, highlighting a key gap in understanding the pathophysiology of ARDS.

In vitro experiments using LPS/ATP-stimulated MH-S macrophages demonstrated characteristic pyroptotic changes, including notable elevation of pyroptosis-related markers (NLRP3, ASC, CASP1 and GSDMD) at both the protein and mRNA levels, increased cell death indicators and the release of mature inflammatory cytokines (IL-18 and IL-1β) into culture supernatants. Notably, CA was revealed to prevent the changes observed in the aforementioned indicators. These *in vitro* findings were corroborated *in vivo* using a mouse model of ARDS. CA administration reduced pulmonary expression of NLRP3 inflammasome components, alveolar damage markers (LDH release), and BALF concentrations of IL-18 and IL-1β. Collectively, these findings suggested airway macrophage pyroptosis as a promising therapeutic target for ARDS intervention, with CA representing a potential NLRP3-targeted therapeutic candidate that warrants further clinical investigation.

Emerging evidence has highlighted a key regulatory relationship between Nrf2 activation and NLRP3 inflammasome suppression across various cell types (45-47). Notably, Nrf2 has been shown to negatively regulate NLRP3 inflammasome activation in primary microglia, attenuating neuroinflammatory responses (48,49), while in cardiomyocytes, Nrf2 similarly modulates ROS-induced NLRP3 activation. To the best of our knowledge, the Nrf-NLRP3 regulatory axis had not been investigated in MH-S cells prior to the present study. The findings of the present study demonstrated that CA simultaneously activated Nrf2 signaling and inhibited NLRP3 inflammasome-mediated pyroptosis in MH-S cells. Through pharmacological inhibition using ML385, a potentially causal relationship was established whereby the Nrf2 blockade abrogated the suppressive effects of CA on NLRP3 activation. These results suggested that CA may exert its protective effects against ARDS through Nrf2-dependent suppression of NLRP3-mediated pyroptosis in alveolar macrophages, revealing a novel therapeutic mechanism for this phytochemical compound.

In conclusion, the present study established that CA exerts potent protective effects against ARDS through a novel dual-mechanism action, activating the Nrf2/HO-1 pathway to alleviate oxidative stress, and inhibiting NLRP3 inflammasome-mediated pyroptosis by blocking CASP1 activation and GSDMD cleavage (Fig. 8). The findings suggested that CA may simultaneously target these two key pathways in MH-S cells, revealing an important Nrf2-NLRP3 regulatory axis in the pathogenesis of ARDS. While the therapeutic potential of CA was established through *in vitro* and *in vivo* validation, further research is necessary to evaluate dose-response relationships, long-term safety profiles, optimal delivery methods and potential drug interactions before clinical translation. The present study not only advances general understanding of ARDS pathophysiology but also provides a foundation for developing plant-derived multi-target therapies for inflammatory lung diseases.

Acknowledgements

Not applicable.

Funding

This work was financially supported by the Suqian Science&Tech Program (grant no. KY202209), the General Project of Science and Technology Development Fund of Nanjing Medical University (grant no. NMUB20210295) and the Suqian City Traditional Chinese Medicine Science and Technology Project (grant no. YB202212).

Availability of data and materials

The data generated in the present study may be requested from the corresponding author.

Authors' contributions

QL contributed to writing the original draft, project administration, methodology, investigation, funding acquisition, formal analysis and data curation. LD contributed to the software used, formal analysis, data curation and visualization. HS contributed to data curation, formal analysis, methodology and writing the original draft. WD contributed to the methodology, data curation, formal analysis and investigation. MW contributed to project administration and data curation. ZS contributed to the study conception and design, data interpretation, and critically revised the manuscript for important intellectual content. CM contributed to the acquisition of funding, project administration, data analysis and interpretation, and critically revised the manuscript. QL and CM confirm the authenticity of all the raw data. All authors have read and approved the final manuscript.

Ethics approval and consent to participate

All experimental procedures involving animals were conducted in strict adherence to the Guide for the Care and Use of Laboratory Animals. Furthermore, the present study protocol was approved by the Institutional Ethics Committee of Jinling Hospital, Medical School of Nanjing University (approval no. 2022DZGKJDWLS-00161).

Patient consent for publication

Not applicable.

Competing interests

The authors declare that they have no competing interests.

References

1. Gorman EA, O'Kane CM and McAuley DF: Acute respiratory distress syndrome in adults: diagnosis, outcomes, long-term sequelae, and management. Lancet 400: 1157-1170, 2022.
2. Wick KD, Ware LB and Matthay MA: Acute respiratory distress syndrome. BMJ 387: e76612, 2024.
3. Matthay MA, Arabi Y, Arroliga AC, Bernard G, Bersten AD, Brochard LJ, Calfee CS, Combes A, Daniel BM, Ferguson ND, *et al*: A new global definition of acute respiratory distress syndrome. Am J Resp Crit Care 209: 37-47, 2024.
4. He YQ, Zhou CC, Yu LY, Wang L, Deng JL, Tao YL, Zhang F and Chen WS: Natural product derived phytochemicals in managing acute lung injury by multiple mechanisms. Pharmacol Res 163: 105224, 2021.
5. Farhadi F, Baradaran Rahimi V, Mohamadi N and Askari VR: Effects of rosmarinic acid, carnosic acid, rosmanol, carnosol, and ursolic acid on the pathogenesis of respiratory diseases. Biofactors 49: 478-501, 2023.
6. McCord JM, Hybertson BM, Cota-Gomez A and Gao B: Nrf2 activator PB125® as a carnosic acid-based therapeutic agent against respiratory viral diseases, including COVID-19. Free Radical Bio Med 175: 56-64, 2021.
7. Zhang D, Lee B, Nutter A, Song P, Dolatabadi N, Parker J, Sanz-Blasco S, Newmeyer T, Ambasudhan R, McKercher SR, *et al*: Protection from cyanide-induced brain injury by the Nrf2 transcriptional activator carnosic acid. J Neurochem 133: 898-908, 2015.
8. Zhang C, Zhao M, Wang B, Su Z, Guo B, Qin L, Zhang W and Zheng R: The Nrf2-NLRP3-caspase-1 axis mediates the neuroprotective effects of Celastrol in Parkinson's disease. Redox Biol 47: 102134, 2021.
9. Arioz BI, Tastan B, Tarakcioglu E, Tufekci KU, Olcum M, Ersoy N, Bagriyanik A, Genc K and Genc S: Melatonin attenuates LPS-Induced acute depressive-like behaviors and microglial NLRP3 inflammasome activation through the SIRT1/Nrf2 pathway. Front Immunol 10: 1511, 2019.
10. Xu L, Zhu Y, Li C, Wang Q, Ma L, Wang J and Zhang S: Small extracellular vesicles derived from Nrf2-overexpressing human amniotic mesenchymal stem cells protect against lipopolysaccharide-induced acute lung injury by inhibiting NLRP3. Biol Direct 17: 35, 2022.
11. Dhar R, Rana MN, Zhang L, Li Y, Li N, Hu Z, Yan C, Wang X, Zheng X, Liu H, *et al*: Phosphodiesterase 4B is required for NLRP3 inflammasome activation by positive feedback with Nrf2 in the early phase of LPS-induced acute lung injury. Free Radical Bio Med 176: 378-391, 2021.
12. Zhou Y, Zhou B, Pache L, Chang M, Khodabakhshi AH, Tanaseichuk O, Benner C and Chanda SK: Metascape provides a biologist-oriented resource for the analysis of systems-level datasets. Nat Commun 10: 1523, 2019.
13. Gene Ontology Consortium: Gene Ontology Consortium: Going forward. Nucleic Acids Res 43(Database issue): D1049-D1056, 2015.
14. Kanehisa M and Goto S: KEGG: Kyoto encyclopedia of genes and genomes. Nucleic Acids Res 28: 27-30, 2000.
15. Shannon P, Markiel A, Ozier O, Baliga NS, Wang JT, Ramage D, Amin N, Schwikowski B and Ideker T: Cytoscape: A software environment for integrated models of biomolecular interaction networks. Genome Res 13: 2498-2504, 2003.
16. Paggi JM, Pandit A and Dror RO: The art and science of molecular docking. Annu Rev Biochem 93: 389-410, 2024.
17. Kaiyun T, Xiaotong X, Min L, Yongrong W, Xuyi T, Fu S, Jinwen G and Gaoyan K: Jiawei duhuo jisheng mixture mitigates osteoarthritis progression in rabbits by inhibiting inflammation: A network pharmacology and experimental approach. Comb Chem High Throughput Screen 28: 2107-2131, 2025.
18. Ding Z, Lu Y, Zhao J, Zhang D and Gao B: Network pharmacology and molecular dynamics identified potential androgen receptor-targeted metabolites in crocus alatavicus. Int J Mol Sci 26: 3533, 2025.
19. Kumari R, Kumar R; Open Source Drug Discovery Consortium; Lynn A: g_mmpbsa-a GROMACS tool for high-throughput MM-PBSA calculations. J Chem Inf Model 54: 1951-1962, 2014.
20. Xuan W, Wu X, Zheng L, Jia H, Zhang X, Zhang X and Cao B: Gut microbiota-derived acetic acids promoted sepsis-induced acute respiratory distress syndrome by delaying neutrophil apoptosis through FABP4. Cell Mol Life Sci 81: 438, 2024.
21. Huang X, Zhu W, Zhang H, Qiu S and Shao H: SARS-CoV-2 N protein induces alveolar epithelial apoptosis via NLRP3 pathway in ARDS. Int Immunopharmacol 144: 113503, 2025.
22. Jeong EJ, Choi JJ, Lee SY and Kim YS: The effects of ML385 on head and neck squamous cell carcinoma: implications for NRF2 inhibition as a therapeutic strategy. Int J Mol Sci 25: 7011, 2024.
23. Chen J, Ding W, Zhang Z, Li Q, Wang M, Feng J, Zhang W, Cao L, Ji X, Nie S and Sun Z: Shenfu injection targets the PI3K-AKT pathway to regulate autophagy and apoptosis in acute respiratory distress syndrome caused by sepsis. Phytomedicine 129: 155627, 2024.
24. McGinn R, Fergusson DA, Stewart DJ, Kristof AS, Barron CC, Thebaud B, McIntyre L, Stacey D, Liepmann M, Dodelet-Devillers A, *et al*: Surrogate humane endpoints in small animal models of acute lung injury: A modified delphi consensus study of researchers and laboratory animal veterinarians. Crit Care Med 49: 311-323, 2021.

25. Zingarelli B: First do no harm: A proposal of an expert-guided framework of surrogate humane endpoints in preclinical models of acute lung injury. Crit Care Med 49: 373-375, 2021.
26. Kang JY, Xu MM, Sun Y, Ding ZX, Wei YY, Zhang DW, Wang YG, Shen JL, Wu HM and Fei GH: Melatonin attenuates LPS-induced pyroptosis in acute lung injury by inhibiting NLRP3-GSDMD pathway via activating Nrf2/HO-1 signaling axis. INT Immunopharmacol 109: 108782, 2022.
27. Livak KJ and Schmittgen TD: Analysis of relative gene expression data using real-time quantitative PCR and the 2(-Delta Delta C(T)) Method. Methods 25: 402-408, 2001.
28. Bahri S, Jameleddine S and Shlyonsky V: Relevance of carnosic acid to the treatment of several health disorders: Molecular targets and mechanisms. Biomed Pharmacother 84: 569-582, 2016.
29. He F, Ru X and Wen T: NRF2, a transcription factor for stress response and beyond. Int J Mol Sci 21: 4777, 2020.
30. Pinela J, Dias MI, Pereira C and Alonso-Esteban JI: Antioxidant activity of foods and natural products. Molecules 29: 1814, 2024.
31. Cardoso SM and Fassio A: The antioxidant capacities of natural products 2019. Molecules 25: 5676, 2020.
32. Qiu Y, Chen S, Yu M, Shi J, Liu J, Li X, Chen J, Sun X, Huang G and Zheng C: Natural products from marine-derived fungi with anti-inflammatory activity. Mar Drugs 22: 433, 2024.
33. Moudgil KD and Venkatesha SH: The anti-inflammatory and immunomodulatory activities of natural products to control autoimmune inflammation. Int J Mol Sci 24: 95, 2022.
34. Heard SC, Wu G and Winter JM: Antifungal natural products. Curr Opin Biotechnol 69: 232-241, 2021.
35. Lewis K, Lee RE, Brötz-Oesterhelt H, Hiller S, Rodnina MV, Schneider T, Weingarth M and Wohlgemuth I: Sophisticated natural products as antibiotics. Nature 632: 39-49, 2024.
36. Amaral-Machado L, Oliveira WN, Rodrigues VM, Albuquerque NA, Alencar ÉN and Egito EST: Could natural products modulate early inflammatory responses, preventing acute respiratory distress syndrome in COVID-19-confirmed patients? Biomed Pharmacother 134: 111143, 2021.
37. Maione F, Cantone V, Pace S, Chini MG, Bisio A, Romussi G, Pieretti S, Werz O, Koeberle A, Mascolo N and Bifulco G: Anti-inflammatory and analgesic activity of carnosol and carnosic acid in vivo and in vitro and in silico analysis of their target interactions. Br J Pharmacol 174: 1497-1508, 2017.
38. Albadrani GM, Altyar AE, Kensara OA, Haridy MAM, Zaazouee MS, Elshanbary AA, Sayed AA and Abdel-Daim MM: Antioxidant, anti-inflammatory, and anti-DNA damage effects of carnosic acid against aflatoxin B1-induced hepatic, renal, and cardiac toxicities in rats. Toxicol Res (Camb) 13: tfae083, 2024.
39. Dhlamini Q, Wang W, Feng G, Chen A, Chong L, Li X, Li Q, Wu J, Zhou D, Wang J, *et al*: FGF1 alleviates LPS-induced acute lung injury via suppression of inflammation and oxidative stress. Mol Med 28: 73, 2022.
40. Gong L, Shen Y, Wang S, Wang X, Ji H, Wu X, Hu L and Zhu L: Nuclear SPHK2/S1P induces oxidative stress and NLRP3 inflammasome activation via promoting p53 acetylation in lipopolysaccharide-induced acute lung injury. Cell Death Discov 9: 12, 2023.
41. Zhu YS, Shah SAA, Yang BY, Fan SS, He L, Sun YR, Shang WB, Qian Y and Zhang X: Gen-17, a beta-methyl derivative of Genipin, attenuates LPS-induced ALI by regulating Keap1-Nrf2/HO-1 and suppressing NF-κB and MAPK-dependent signaling pathways. Biochim Biophys Acta Mol Basis Dis 1871: 167770, 2025.
42. Huang J, Zhu Y, Li S, Jiang H, Chen N, Xiao H, Liu J, Liang D, Zheng Q, Tang J and Meng X: Licochalcone B confers protective effects against LPS-Induced acute lung injury in cells and mice through the Keap1/Nrf2 pathway. Redox Rep 28: 2243423, 2023.
43. Song Y, Gou Y, Gao J, Chen D, Zhang H, Zhao W, Qian F, Xu A and Shen Y: Lomerizine attenuates LPS-induced acute lung injury by inhibiting the macrophage activation through reducing Ca(2+) influx. Front Pharmacol 14: 1236469, 2023.
44. Sayson SG, Ashbaugh A, Porollo A, Smulian G and Cushion MT: Pneumocystis murina promotes inflammasome formation and NETosis during Pneumocystis pneumonia. mBio 15: e140924, 2024.
45. Che J, Wang H, Dong J, Wu Y, Zhang H, Fu L and Zhang J: Human umbilical cord mesenchymal stem cell-derived exosomes attenuate neuroinflammation and oxidative stress through the NRF2/NF-κB/NLRP3 pathway. CNS Neurosci Ther 30: e14454, 2024.
46. Rajan S, Tryphena KP, Khan S, Vora L, Srivastava S, Singh SB and Khatri DK: Understanding the involvement of innate immunity and the Nrf2-NLRP3 axis on mitochondrial health in Parkinson's disease. Ageing Res Rev 87: 101915, 2023.
47. Sun YY, Zhu HJ, Zhao RY, Zhou SY, Wang MQ, Yang Y and Guo ZN: Remote ischemic conditioning attenuates oxidative stress and inflammation via the Nrf2/HO-1 pathway in MCAO mice. Redox Biol 66: 102852, 2023.
48. Han QQ and Le W: NLRP3 inflammasome-mediated neuroinflammation and related mitochondrial impairment in Parkinson's disease. Neurosci Bull 39: 832-844, 2023.
49. Qiu WQ, Ai W, Zhu FD, Zhang Y, Guo MS, Law BY, Wu JM, Wong VK, Tang Y, Yu L, *et al*: Polygala saponins inhibit NLRP3 inflammasome-mediated neuroinflammation via SHP-2-Mediated mitophagy. Free Radical Bio Med 179: 76-94, 2022.